



Cite this: *Phys. Chem. Chem. Phys.*,  
2020, 22, 10278

## Effects of radial injection and solution thickness on the dynamics of confined $A + B \rightarrow C$ chemical fronts

Ágota Tóth,<sup>a</sup> Gábor Schuszter,<sup>a</sup> Nirmali Prabha Das,<sup>a</sup> Emese Lantos,<sup>a</sup>  
Dezső Horváth,<sup>b</sup> A. De Wit<sup>c</sup> and Fabian Brau<sup>\*c</sup>

The spatio-temporal dynamics of an  $A + B \rightarrow C$  front subjected to radial advection is investigated experimentally in a thin solution layer confined between two horizontal plates by radially injecting a solution of potassium thiocyanate (A) into a solution of iron(III) nitrate (B). The total amount and spatial distribution of the product  $\text{FeSCN}^{2+}$  (C) are measured for various flow rates  $Q$  and solution thicknesses  $h$ . The long-time evolution of the total amount of product,  $n_C$ , is compared to a scaling obtained theoretically from a one-dimensional reaction–diffusion–advection model with passive advection along the radial coordinate  $r$ . We show that, in the experiments,  $n_C$  is significantly affected when varying either  $Q$  or  $h$  but scales as  $n_C \sim Q^{-1/2}V$  where  $V$  is the volume of injected reactant A provided the solution thickness  $h$  between the two confining plates is sufficiently small, in agreement with the theoretical prediction. Our experimental results also evidence that the temporal evolution of the width of the product zone,  $W_C$ , follows a power law, the exponent of which varies with both  $Q$  and  $h$ , in disagreement with the one-dimensional model that predicts  $W_C \sim t^{1/2}$ . We show that this experimental observation can be rationalized by taking into account the non-uniform profile of the velocity field of the injected reactant within the cell gap.

Received 25th November 2019,  
Accepted 19th April 2020

DOI: 10.1039/c9cp06370f

rsc.li/pccp

## 1 Introduction

Reaction–diffusion (RD) models<sup>1</sup> can describe dynamics in a wide variety of systems ranging from population dynamics,<sup>2</sup> disease spreading,<sup>3</sup> epidemiology,<sup>4</sup> ecology,<sup>5</sup> and biological pattern formation<sup>6</sup> to upper atmospheric lightning,<sup>7</sup> finance<sup>8</sup> and particle physics,<sup>9</sup> to name a few. In many cases, RD fronts can form when two species A and B are initially separated and meet by diffusion, react and form a product C. Such  $A + B \rightarrow C$  fronts have been intensively studied in one-dimensional (1D) rectilinear geometries for which the initial contact zone between A and B is a line. Scalings of the temporal evolution of the front position as well as of the amplitude and width of the production rate (defined as  $R = kab$ , where  $a$  and  $b$  are the concentrations of the species A and B and  $k$  is the rate constant of the reaction) have been derived theoretically<sup>10</sup> and tested both numerically<sup>11</sup> and experimentally using chemical reactions.<sup>12–14</sup>

Recently, this  $A + B \rightarrow C$  RD front theory has been extended to radial geometries with advection when A is injected radially into B at a given flow rate  $Q$ .<sup>15</sup> Assuming no transverse deformation and a plug flow along the thickness  $h$  of the solution along the  $z$ -axis, see Fig. 1(b), this 1D theory provides the temporal evolution of the position  $r_f$  of the front and of the amplitude  $R(r_f)$  and width  $w$  of the production rate  $R$  in the asymptotic long time limit. This limit is obtained when  $ka_0t \gg (hD/Q)^{3/4}$ , where  $a_0$  is the initial concentration of A,  $t$  is the time,  $Q$  is the volumetric flow rate, and  $D$  is the molecular diffusion coefficient assumed equal for all species. It has been shown that, in this limit, the properties of the front scale as  $r_f = \alpha(Q, \gamma)t^{1/2}$ ,  $R(r_f) = \beta(Q, \gamma)t^{-2/3}$  and  $w = \delta(Q, \gamma)t^{1/6}$ , where  $\alpha$ ,  $\beta$  and  $\delta$  are known functions of  $Q$  and of  $\gamma = b_0/a_0$  with  $b_0$  the initial concentration of B.<sup>15,16</sup> These scalings are similar to those obtained in a rectilinear geometry except for the non-trivial dependence on the flow rate  $Q$ . The major difference introduced by the radial geometry appears in the temporal evolution of the total amount of product  $n_C$ . Indeed, in a rectilinear geometry,  $n_C \sim a_0hL(Dt)^{1/2}$ , where  $L$  is the constant length of the contact zone between the two reactants A and B, whereas, in a radial geometry,  $n_C \sim a_0j(\gamma)h(Q/hD)^{1/2}(Dt)$ , where  $j(\gamma) \simeq [\ln(4.5\gamma + 1)]/3$  for  $0.1 \lesssim \gamma \lesssim 10$ . This difference originates primarily from the growth in time of the length  $L$

<sup>a</sup> Department of Physical Chemistry and Materials Science, University of Szeged,  
Rerrich Béla tér 1., Szeged, H-6720, Hungary

<sup>b</sup> Department of Applied and Environmental Chemistry, University of Szeged,  
Rerrich Béla tér 1., Szeged, H-6720, Hungary

<sup>c</sup> Université libre de Bruxelles (ULB), Nonlinear Physical Chemistry Unit, Faculté des  
Sciences, CP-231, 1050 Brussels, Belgium. E-mail: fabian.brau@ulb.ac.be

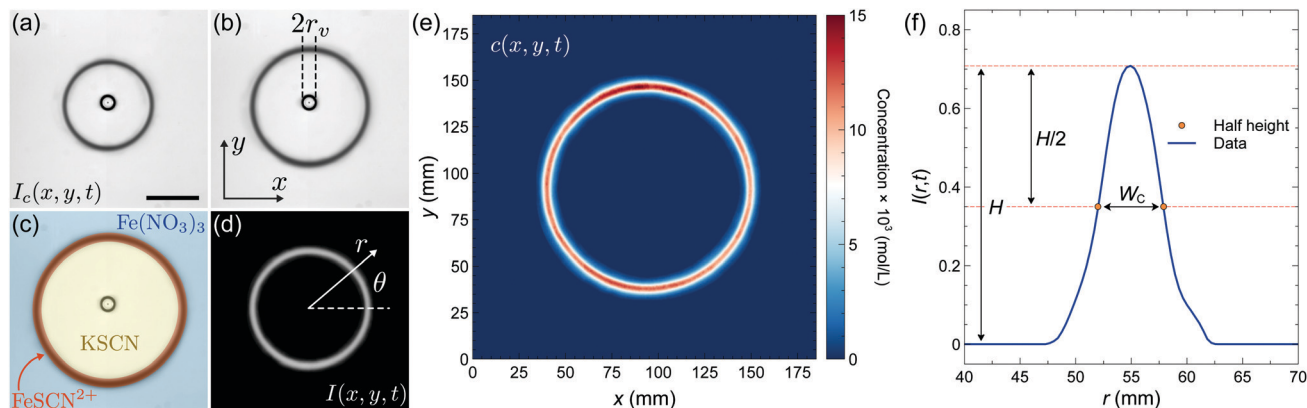


**Fig. 1** (a)–(c) Snapshots of the coloured ring of the product in an injection experiment at  $t = 1121, 1881,$  and  $3021$  s with flow rate  $Q = 0.05$  ml  $\text{min}^{-1}$  and solution thickness  $h = 0.66$  mm. Image (c) is displayed in false colors to show the respective locations of the two reactants and of the product. The small circle at the center of the images is the injection valve. Scale bar 5 cm. (d) Grayscale intensity  $I(x, y, t)$  obtained after subtracting the image at  $t = 0$  from image (b). (e) Concentration distribution of image (b) computed from image (d) and a calibration curve. (f) Radial profile,  $I(r, t)$ , of the grayscale intensity of image (d) showing the width of the product zone,  $W_C$ , measured at half the height of the peak.

of the contact zone between the two reactants in the radial geometry as:<sup>16</sup>  $L = 2\pi r_f \sim t^{1/2}$ . Since, by definition of the flow rate, the injected volume,  $V$ , evolves in time as  $V = Qt$ , this scaling can be written as

$$n_C = \eta a_0 j(\gamma) [hD/Q]^{1/2} V, \quad (1)$$

where  $\eta$  is a numerical constant. This scaling has been tested experimentally using calcium carbonate precipitation as a model reaction.<sup>15</sup> For given parameter values ( $a_0$ ,  $\gamma$ ,  $D$ , and  $h$ ), the experimental evolution of  $n_C$  with  $Q$  and  $V$  was measured to be  $n_C \sim Q^{-0.4} V$ . The slightly larger value of the exponent in the experiments, *i.e.*,  $-0.4$  instead of  $-1/2$ , implies that the production of calcium carbonate decreases slightly less compared to the theoretical prediction when  $Q$  increases. This discrepancy was attributed to undetected buoyancy-driven convection due to the density difference between the precipitate and the surrounding solution, which enhances the mixing and hence the production of the precipitate.

To reduce the density difference between the product and the reactants, we test experimentally here the theoretical scaling (1) using the complex formation of  $\text{FeSCN}^{2+}$  between the reactants potassium thiocyanate KSCN (A) and iron(III) nitrate  $\text{Fe}(\text{NO}_3)_3$  (B) in the presence of radial injection as a model reaction for  $A + B \rightarrow C$  processes. The selected reaction is very fast and yields a product “instantly” when the two colorless reactants are in contact. The long-time limit for which the scaling (1) is valid is thus reached soon after injection starts. Moreover, the product is characterized by a prominent brown color allowing us to easily visualize the front, as shown in Fig. 1(a–c). The theory is further tested by measuring the width of the product zone,  $W_C$ , as a function of time. In the long-time limit, this quantity should evolve as  $W_C \sim t^\varepsilon$ , with  $\varepsilon = 1/2$  for a one-dimensional dynamics neglecting any spatial variation within the thickness of the solution. We observe however that the exponent varies with both  $Q$  and  $h$  and is sub-diffusive, *i.e.*,  $\varepsilon < 1/2$ . We show that this result can be

rationalized by taking into account the three-dimensional profile of the velocity field of the injected reactant within the reactor gap.

## 2 Experimental methods

Reagent-grade chemicals (Alfa-Aesar, VWR) are used throughout the experiments without further purification. The experiments are performed in the quasi two-dimensional confined geometry of a horizontal Hele-Shaw cell consisting of two transparent glass plates separated by a small gap  $h$ . This gap that fixes the solution thickness  $h$  is controlled using spacers ranging from  $h = (0.18 \pm 0.03)$  mm to  $h = (0.66 \pm 0.06)$  mm. In such a thin layer, both reactant solutions appear colorless whereas the product has a well visible brown color, see Fig. 1(a–c). The setup is illuminated from above by two light sources and the dynamics is recorded using a digital camera. The gap between the two plates of the cell is initially filled with an aqueous solution of iron(III) nitrate  $\text{Fe}(\text{NO}_3)_3$  (0.03 M), which is acidified with 0.174 ml of a  $\text{HNO}_3$  solution at 0.1 M per 25 ml of solution to stabilize  $\text{Fe}^{3+}$  ions. An aqueous solution of potassium thiocyanate KSCN (0.03 M) is then radially injected through the center of the lower plate using a syringe pump (KD Scientific) at a constant flow rate  $Q$ , ranging from 0.01 to 0.09 ml  $\text{min}^{-1}$ . The low concentrations of the two reactants induce small differences of viscosity ( $\mu_{\text{Fe}(\text{NO}_3)_3} = (0.98 \pm 0.01)$  mPa s and  $\mu_{\text{KSCN}} = (1.03 \pm 0.01)$  mPa s) and of density ( $\rho_{\text{Fe}(\text{NO}_3)_3} = (1.0068 \pm 0.0001)$  g  $\text{cm}^{-3}$  and  $\rho_{\text{KSCN}} = (0.9993 \pm 0.0001)$  g  $\text{cm}^{-3}$ ). Together with the low flow rates used, this prevents the emergence of transverse hydrodynamic instabilities, which preserves the radial symmetry, see Fig. 1(a–c). The dynamics is thus at most two-dimensional. Small gaps of  $h$  are used to approach a one-dimensional dynamics to get closer to the assumption made in the theory<sup>15</sup> used to derive the scaling (1). When the two reactants are in contact, depending on the stoichiometric ratio of the reactants, a number of  $\text{Fe}(\text{SCN})_i^{3-i}$  complexes,

where  $i$  ranges from 1 to 6, can be obtained. The concentrations of both reactants and the way the injection is performed, *i.e.*,  $\text{SCN}^-$  into  $\text{Fe}^{3+}$ , are chosen such that the mono-complex  $\text{FeSCN}^{2+}$  is the dominant product. In addition, we have  $\text{SCN}^- + \text{Fe}^{3+} \xrightleftharpoons[k']{k} \text{FeSCN}^{2+}$ , with  $k \simeq 200 \text{ M}^{-1} \text{ s}^{-1}$  and  $k' \simeq 1.5 \text{ s}^{-1}$ .<sup>17</sup> Therefore, the equilibrium is strongly shifted towards the product, as required to compare with the theory.<sup>15</sup>

The concentration distribution of the product of the reaction,  $c(x,y,t)$ , where  $x$  and  $y$  are the spatial coordinates in the horizontal plane, is reconstructed from the recorded images of the dynamics in order to test the scaling (1). For this purpose, we measure the local grayscale intensity,  $I_0(x,y)$ , of the background image of the cell containing only  $\text{Fe}(\text{NO}_3)_3$ , *i.e.*, before injection starts. The average value,  $I_0$ , of this essentially uniform distribution is also computed in a region  $r > r_v$ , where  $r$  is the radial distance measured from the center of the injection zone and  $r_v$  is the radius of the injection valve, see Fig. 1(b). At times  $t_n = n\Delta t$ , where  $n$  is an integer, the local grayscale intensity,  $I_c(x,y,t)$ , of the images of the dynamics is measured, see Fig. 1(a–c). The local relative grayscale intensity, obtained after subtracting the grayscale intensity of the background image, is then computed using the relation

$$I(x,y,t) = [I_0(x,y) - I_c(x,y,t)]/I_0. \quad (2)$$

An example of this relative distribution of intensity is shown in Fig. 1(d). Fig. 1(e) shows the local concentration field computed from  $I(x,y,t)$  shown in Fig. 1(d) by using a calibration curve, see Appendix A. Notice that, in these experiments, only the concentration field averaged over the reactor gap can be reconstructed, *i.e.*,  $c(x,y,t) \equiv h^{-1} \int_0^h c(x,y,z,t) dz$ . The total amount of product,  $n_C$ , is then obtained by integrating the concentration distribution over the entire image:

$$n_C(t) = \int c(x,y,t) dx dy. \quad (3)$$

Finally, the width of the product concentration field,  $W_C$ , is defined as the width at half-height of the radial grayscale intensity profile,  $I(r,t)$ , where  $r$  is the radial distance measured from the center of injection, see Fig. 1(d) and (f). This radial profile,  $I(r,t)$ , is obtained by measuring the intensity  $I$  along radial lines separated by  $\Delta\theta \simeq 0.02$  and averaging over the polar angle  $\theta$ .

## 3 Results and discussions

### 3.1 Total amount of product

The 1D reaction–diffusion–advection (RDA) theory for  $A + B \rightarrow C$  fronts subject to passive radial advection<sup>15</sup> predicts that the total amount of product,  $n_C$ , grows linearly with the injected volume of reactant A as

$$n_C = S_{\text{th}}V + p, \quad (4)$$

where  $p$  is a constant and  $S_{\text{th}}$  is the theoretical slope varying with the flow rate as

$$S_{\text{th}} = \alpha Q^{-1/2} \quad (5)$$

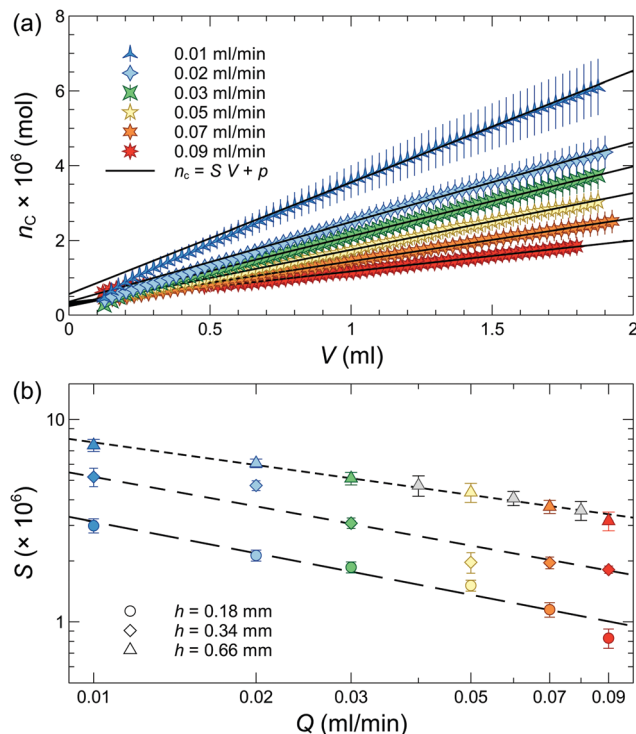


Fig. 2 (a) Total amount of product  $n_C$  as a function of the volume  $V$  of KSCN solution injected for six different flow rates and  $h = 0.18$  mm. The evolution of  $n_C(V)$  is similar for other  $h$  and is not displayed. (b) Slope  $S$ , measured from panel (a), as a function of the flow rate  $Q$  for various solution heights. The dashed lines are fitted power laws:  $S = \alpha Q^{-\beta}$ .

where  $\alpha$  is a parameter independent of  $Q$ . The typical evolution of  $n_C$  obtained experimentally as a function of the volume of KSCN injected is shown in Fig. 2(a) for some values of the flow rate and one value of the solution thickness  $h$ . These data result from the average over at least three experiments performed for each value of  $Q$  and  $h$ . We see that, after some transient evolution,  $n_C$  evolves indeed linearly with  $V$  in agreement with the theoretical scaling (4). The slope  $S$  was extracted from linear regressions performed at sufficiently large injected volumes, as shown in Fig. 2(a). The evolution of  $S$  as a function of  $Q$  is shown in Fig. 2(b) for three different values of  $h$ . The uncertainties in  $S$  result from the errors displayed in Fig. 2(a) whereas the errors in the flow rate  $Q$  are neglected.

In the experiments, the dependence of  $S$  on the flow rate is well described by a power law  $S = \alpha Q^{-\beta}$ , as predicted by eqn (5). Nevertheless, instead of the predicted constant theoretical value  $\beta = 1/2$ , we find that the experimental value of the exponent  $\beta$  varies with the solution height  $h$  as shown in Table 1, approaching the value  $1/2$  only as  $h$  decreases. At larger  $h$ ,

Table 1 Fitted parameters of the power law  $S = \alpha Q^{-\beta}$  shown in Fig. 2(b) for different solution heights

$h$ (mm)	$\alpha \times 10^6$ (mol ml <sup>-1</sup> min <sup>-β</sup> )	$\beta$
0.18 ± 0.03	0.29 ± 0.04	0.52 ± 0.04
0.34 ± 0.05	0.56 ± 0.07	0.48 ± 0.04
0.66 ± 0.06	1.38 ± 0.17	0.37 ± 0.04

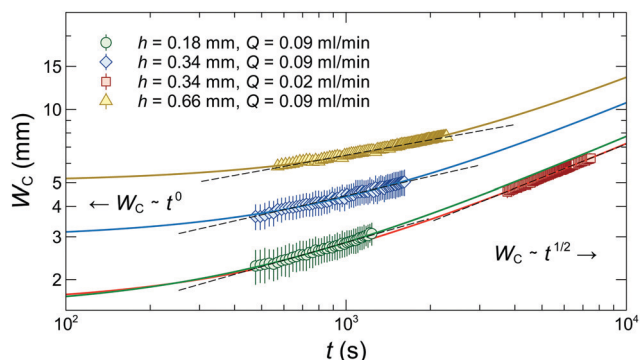


Fig. 3 Width of the product distribution as a function of time for various solution height  $h$  and flow rate  $Q$ . Dashed lines indicate fitted curves according to the power law  $W = \delta t^\epsilon$ . Solid curves indicate fits to the data according to eqn (12). The values of the fitting parameters, namely  $\delta$ ,  $\epsilon$ ,  $W_C^0$  and  $t_c$ , are reported in Table 2.

the exponent decreases below the theoretical value while the coefficient  $\alpha$  increases, in agreement with what has been measured experimentally previously using a precipitation reaction.<sup>15</sup> This means that, for larger gaps, more product is generated when the flow rate increases than expected from the 1D theory assuming a plug flow within the gap. This suggests that extra mixing develops within the reactor gap on increasing the solution height, yielding a more efficient contact between the reactants that enhances the production of the complex.

To sum up, these experimental results confirm thus that provided the solution height is sufficiently small and the radial symmetry is preserved to approach a 1D plug flow dynamics, the total amount of product generated in a radial injection follows the theoretical scaling (4). At larger gaps, however, additional effects induce an enhanced production of C.

### 3.2 Width of the product zone

The local dynamics of the front can be further analyzed by measuring the temporal evolution of the width  $W_C$  of the product zone, which should evolve as  $W_C \sim t^{1/2}$  according to the theory.<sup>15</sup> The experimental evolution of  $W_C$  is shown in Fig. 3 for various flow rates and cell gaps. In all cases, the width evolves in time following a power law:  $W_C = \delta t^\epsilon$ , as predicted theoretically. Nevertheless, the values of the coefficient  $\delta$  and

Table 2 Fitted parameters of the power law  $W_C = \delta t^\epsilon$  and of eqn (12) shown in Fig. 3 for different solution heights  $h$  and flow rates  $Q$

$h$ (mm)	$Q$ (ml min <sup>-1</sup> )	$\delta$ (mm s <sup>-<math>\epsilon</math>)</sup>	$\epsilon$
0.18 ± 0.03	0.09	0.291 ± 0.011	0.330 ± 0.005
0.34 ± 0.05	0.09	0.727 ± 0.017	0.261 ± 0.003
0.34 ± 0.05	0.02	0.108 ± 0.001	0.456 ± 0.002
0.66 ± 0.06	0.09	1.534 ± 0.019	0.209 ± 0.002
$h$ (mm)	$Q$ (ml min <sup>-1</sup> )	$W_C^0$ (mm)	$t_c$ (s)
0.18 ± 0.03	0.09	1.54 ± 0.02	412 ± 15
0.34 ± 0.05	0.09	2.98 ± 0.03	856 ± 28
0.34 ± 0.05	0.02	1.60 ± 0.03	511 ± 20
0.66 ± 0.06	0.09	5.15 ± 0.02	1753 ± 23

the exponent  $\epsilon$  vary experimentally with  $Q$  and  $h$ , as shown in Table 2. Such a variation of the exponent, whose values are moreover systematically sub-diffusive ( $\epsilon < 1/2$ ), is not expected, since  $W_C$  should grow proportionally to the width of the depletion zone,  $W_d$ , where the concentrations of the two reactants differ significantly from their initial values due to the reaction and diffusion. This depletion zone is known to grow as  $W_d \sim t^{1/2}$  even when there is some advection.<sup>10,15</sup>

In order to rationalize this striking observation, we note that, in the presence of advection, the velocity profile within the reactor gap is not uniform along the vertical  $z$ -axis but is instead described by a Poiseuille profile:<sup>18,19</sup>

$$v_r(r, z) = v_m(r) \left[ 1 - \frac{4z^2}{h^2} \right], \text{ and } v_m(r) = \frac{3Q}{4\pi hr}, \quad (6)$$

where  $z$  varies in the range  $-h/2 \leq z \leq h/2$  and  $v_m$  is the maximum of the velocity profile at  $z = 0$ , which decreases when the radial distance from the injection zone increases. The derivation of this relation together with a discussion of its domain of validity are presented in Appendix B for completeness. In particular, we show that it is valid for a stationary Stokes flow, which neglects the inertial contribution. Under our experimental conditions, this approximation is valid when  $t \gg 0.03$  s.

Eqn (6) shows that decreasing  $h$  increases the velocity gradient along the cell gap since  $\partial_z v_r \sim h^{-2}$ . Therefore, while a global property of the front, such as the total amount of product generated,  $n_C$ , is well described by a one-dimensional model once the cell gap  $h$  is sufficiently small, a local property of the front, such as the width of the product distribution, is increasingly impacted as the gap is decreased and the inhomogeneity of the velocity field along the gap increases. Indeed, eqn (6) shows that fluid particles at different  $z$  positions within the reactor gap travel at different speeds. This shear flow, which increases the spatial spreading of a species, impacts the width of the product zone. This effect can be taken into account through an effective diffusion coefficient,  $D_{\text{eff}}$ , also called the dispersion coefficient, which is given by

$$D_{\text{eff}} = D \left[ 1 + \frac{L^2 U^2}{\sigma D^2} \right], \quad (7)$$

where  $D$  is the molecular diffusion coefficient,  $U$  is the intensity of the gap averaged velocity,  $L$  is the characteristic length of the flow and  $\sigma$  is a numerical factor that depends on the geometry. As shown by Taylor<sup>20</sup> and Aris,<sup>21</sup> in a tube of diameter  $d$ ,  $L = d$  and  $\sigma = 192$ . In a Hele-Shaw cell with rectilinear displacement geometry,  $L = h$  and  $\sigma = 210$ , where  $h$  is the cell gap.<sup>22</sup> We assume here that eqn (7) still applies at sufficiently large times in a Hele-Shaw cell with radial displacement geometry with again  $L = h$  and  $\sigma = 210$ . Therefore, the width of the product zone subjected to dispersion should grow in time as

$$W_C = \xi [D_{\text{eff}} t]^{1/2} = \xi \left[ Dt + \frac{h^2 U^2}{210 D} t \right]^{1/2}, \quad (8)$$

where  $\zeta$  is a numerical constant of order 1. In our case, the gap averaged velocity reads

$$U(r) = \frac{1}{h} \int_{-h/2}^{h/2} v_r(r, z) dz = \frac{2}{3} v_m(r) = \frac{Q}{2\pi hr}. \quad (9)$$

The average front position is thus the solution of the following differential equation

$$\frac{dr}{dt} = U(r) = \frac{Q}{2\pi hr} \Rightarrow r(t) = \left[ \frac{Qt}{\pi h} \right]^{1/2}. \quad (10)$$

The gap averaged velocity of the flow can then be expressed as a function of time as

$$U(t) = U(r(t)) = \frac{1}{2} \left[ \frac{Q}{\pi h} \right]^{1/2} t^{-1/2}. \quad (11)$$

Substituting eqn (11) into eqn (8), we finally obtain the temporal evolution of the width of the product zone taking into account dispersion due to the non-uniformity of the velocity field across the reactor gap:

$$W_C(t) = W_C^0 \left[ 1 + \frac{t}{t_c} \right]^{1/2}, \quad (12a)$$

$$\text{where } t_c = \frac{hQ}{840\pi D^2}, \quad W_C^0 = \xi [Dt_c]^{1/2}. \quad (12b)$$

Relation (12) is not a power law but is characterized by two distinct regimes, at small and large times, which are power laws:

$$W_C^{\text{disp}} \underset{t \ll t_c}{=} W_C^0, \quad \text{and} \quad W_C^{\text{diff}} \underset{t \gg t_c}{=} \xi [Dt]^{1/2}. \quad (13)$$

At small times, dispersion is dominant and leads to  $W_C = W_C^{\text{disp}} = W_C^0$ . As time increases, the front velocity (11) decreases due to volume conservation and dispersion becomes progressively negligible in comparison to molecular diffusion. At large times, diffusion is thus dominant and leads to  $W_C = W_C^{\text{diff}} = W_C^0(t/t_c)^{1/2}$ .

Fig. 3 and Table 2 show that, when  $W_C^0$  and  $t_c$  are considered as independent parameters, the temporal evolution of the width  $W_C$  is well described by eqn (12), without the need to use sub-diffusive exponents varying with  $Q$  and  $h$ . This evidences that the power laws followed by the temporal evolution of  $W_C$  in Fig. 3 correspond actually to a transient regime between the two asymptotic, respectively dispersive and diffusive regimes (13), which are, in contrast, characterized by well-defined power laws. In between these two asymptotic regimes, the exponent obtained by fitting the data by a power law can thus vary between 0 and 1/2. The exponent will be close to 0 (1/2) if the time interval during which the experiment is performed is small (large) compared to  $t_c$ .

Using the mean value of  $h$  and  $t_c$  reported in Table 2, the expression (12b) of  $t_c$  yields a diffusion coefficient of the order of  $D = (0.4 \pm 0.1) \times 10^{-9} \text{ m}^2 \text{ s}^{-1}$ , which is the correct order of magnitude. In addition, eqn (12b) predicts that  $t_c$  and  $W_C^0$  increase with  $h$  and  $Q$  in agreement with the values obtained from the fits shown in Fig. 3 and reported in Table 2.

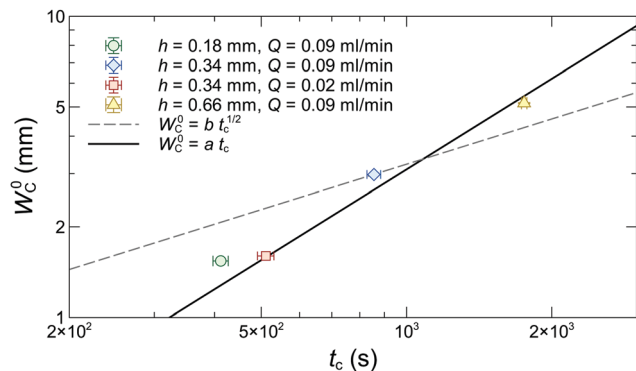


Fig. 4 Evolution of  $W_C^0$  as a function of  $t_c$  together with a linear fit:  $W_C^0 = at_c$  and  $a = 3.1 \mu\text{m s}^{-1}$ , and with eqn (12b) and  $b = \zeta D^{1/2} = 102 \mu\text{m s}^{-1/2}$ .

The relation (12b) between  $W_C^0$  and  $t_c$  provides a more stringent test of the argument used to explain the temporal evolution of  $W_C$ . Indeed, Fig. 4 shows that  $W_C^0$  increases with  $t_c$  following a power law in agreement with eqn (12b). The fit of the data using eqn (12b) yields  $\zeta D^{1/2} = 102 \mu\text{m s}^{-1/2}$ . Using the value of  $D$  obtained above from  $t_c$ , we find that  $\zeta$  is indeed of order  $1:4.4 \lesssim \zeta \lesssim 5.6$ . However, a larger exponent, *i.e.*, 1 instead of 1/2, better describes the evolution of  $W_C^0$  with  $t_c$ . This discrepancy could originate from various factors not taken into account to derive eqn (12), like, for example, the slight difference in density and viscosity between the product and reactant solutions. In addition, the standard theory of dispersion used to obtain the general eqn (7), from which eqn (12) is derived, does not take into account the production of  $C$  due to the chemical reaction. This additional contribution is expected to increase the width of the product zone and could explain the larger exponent obtained in Fig. 4. The extension of the dispersion theory taking into account the production of  $C$  by a chemical reaction is beyond the scope of this work and is left for a subsequent paper.

## 4 Conclusion

The complex formation of  $\text{FeSCN}^{2+}$  has been studied experimentally by radially injecting potassium thiocyanate into iron(III) nitrate in a horizontal Hele-Shaw cell to test the predictions of a recently developed 1D RDA theory of  $A + B \rightarrow C$  fronts in a radial geometry.<sup>15</sup> We have shown that, as predicted theoretically, the total amount of product measured experimentally grows linearly with the volume of injected reactant. In addition, provided the cell gap is small enough, the slope of this linear growth scales as  $Q^{-1/2}$ , where  $Q$  is the volumetric injection rate, in agreement with the 1D theory assuming a plug flow in the gap of the cell. However, at larger gaps, more product is generated than expected and the exponent decreases below the theoretical value, suggesting that enhanced mixing takes place because of a non-uniformity of the velocity field in the gap. We have also measured the dependence of the width  $W_C$  of the product distribution on the flow rate  $Q$  and solution thickness  $h$ . We find that the 1D plug flow model fails to explain the

experimental trends while a 2D simple model taking into account the Poiseuille deformation of the velocity field within the gap of the cell better fits the data. This 2D model suggests that, at small times, the width of the product zone is controlled by dispersion while at larger times when the intensity of advection decreases, a diffusive regime is reached. A preliminary theoretical analysis indicates that the characteristic transition time between the dispersive and diffusive regimes  $t_c \sim hQ/D^2$ , where  $D$  is the molecular diffusion coefficient. The experimental data measured in this transition time between the two asymptotic regimes feature unusual  $W_C = \delta t^\varepsilon$  scalings with a sub-diffusive exponent  $\varepsilon$  that varies with  $Q$  and  $h$ .

Note that decreasing the reactor gap  $h$  allows us to recover the 1D plug flow theoretical scalings for the total amount of product  $n_C$  while increasing the dispersive influence on the local width of the front  $W_C$ . This is related to the fact that  $n_C$  is a global quantity while  $W_C$  is a local property much influenced by the non-uniformity of the velocity field since the gradient of the Poiseuille profile along the reactor gap scales as  $h^{-2}$ . Note that the 2D theory does not take into account the continuous generation of product from the reaction, which could influence dispersion. Moreover, here, we have not addressed the possible influence of convective mixing that could still arise because of slight density differences between the reactant and product solutions. Our experimental results thus clearly show the need for additional experimental and theoretical work aiming to decipher the relative contribution of the reaction, diffusion, dispersion and buoyancy-driven convection to the properties of  $A + B \rightarrow C$  fronts.

## Conflicts of interest

There are no conflicts of interest to declare.

## Appendix

### A Calibration curve

In order to determine the relationship between the grayscale intensity of the  $\text{FeSCN}^{2+}$  complex formed by the reaction and its concentration, the Hele-Shaw cell has been filled by the product solution at various known concentrations  $c$ . The grayscale intensity of the image of the cell filled with the product solution at a given concentration,  $I_c(x,y)$ , has been subtracted from the grayscale intensity of the image of the cell filled with pure water ( $c = 0$ ),  $I_0(x,y)$ . Since both grayscale intensities are essentially uniform over the cell, the resulting grayscale intensity,  $I_0 - I_c$ , is also essentially uniform and vanishes when  $c = 0$ . The relative grayscale intensity of a pixel is then computed as follows:

$$I = \frac{\sum_{i=1}^N [I_0(x_i, y_i) - I_c(x_i, y_i)]}{\sum_{i=1}^N I_0(x_i, y_i)} \equiv \frac{I_0 - I_c}{I_0}, \quad (14)$$

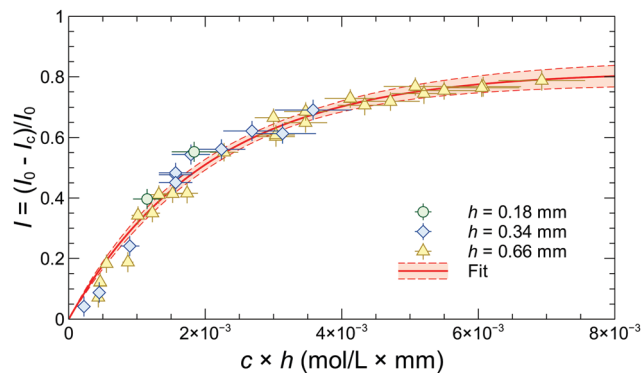


Fig. 5 Evolution of the relative grayscale intensity of a pixel of an image of the cell filled with the complex of  $\text{FeSCN}^{2+}$ , computed using eqn (14), as a function of the concentration of  $\text{FeSCN}^{2+}$  for various reactor gaps. The fit by eqn (16) is also shown together with the 95% confidence band.

where  $N$  is the total number of pixels,  $(x_i, y_i)$  are the coordinates of the pixel  $i$ , and  $I_0$  and  $I_c$  are the average grayscale intensities of a pixel at  $c = 0$  and at a given concentration  $c$ , respectively:

$$I_0 = N^{-1} \sum_{i=1}^N I_0(x_i, y_i), \quad I_c = N^{-1} \sum_{i=1}^N I_c(x_i, y_i). \quad (15)$$

The evolution of  $I$  as a function of the concentration  $c$  of the product is shown in Fig. 5. We observe a good overlapping of the data obtained at various gap  $h$ . These data are well fitted by

$$I = I_\infty (1 - e^{-\kappa c h}), \quad (16)$$

where  $I_\infty = 0.82 \pm 0.02$  and  $\kappa = (488.2 \pm 23.4) \text{ L mol}^{-1} \text{ mm}^{-1}$ .

During a reactive experiment, where potassium thiocyanate is injected into iron(III) nitrate, the grayscale intensity of the cell filled by pure water,  $I_0(x,y)$ , is approximated by the grayscale intensity of the cell filled by  $\text{Fe}(\text{NO}_3)_3$ . Indeed, the concentration of the solution of  $\text{Fe}(\text{NO}_3)_3$  and the reactor gap  $h$  are so small that the solution appears colorless in the reactor and the signal recorded by the camera is indistinguishable from the one recorded with the cell filled by water. The relative grayscale intensity of each pixel,  $I(x_i, y_i, t)$ , is computed using eqn (2). The local concentration at each pixel is then computed using the inverse of eqn (16):

$$c(x_i, y_i, t) = (\kappa h)^{-1} \ln \left( \frac{I_\infty}{I_\infty - I(x_i, y_i, t)} \right). \quad (17)$$

### B Laminar radial flow between two parallel plates

We recall the derivation of the exact solution of the velocity profile, obtained using the Stokes approximation, for a laminar radial flow confined between two parallel plates.<sup>18,19</sup> In the following derivation, we neglect the difference of viscosity and density between the two reactants. We thus consider a single phase, which is a good approximation as the relative difference of density of this horizontal system,  $(\rho_1 - \rho_2)/(\rho_1 + \rho_2)$ , is about

$4 \times 10^{-3}$  and the relative difference of viscosity,  $(\mu_1 - \mu_2)/(\mu_1 + \mu_2)$ , is about  $2 \times 10^{-2}$ .

The Navier–Stokes equations for incompressible Newtonian fluids read

$$\partial_t \mathbf{v} + (\mathbf{v} \cdot \nabla) \mathbf{v} = -\frac{\nabla p}{\rho} + \frac{\mu}{\rho} \nabla^2 \mathbf{v}, \quad (18a)$$

$$\nabla \cdot \mathbf{v} = 0, \quad (18b)$$

where  $\mu$  is the dynamic viscosity and  $\rho$  is the mass density. Since the cell is horizontal, gravity will not impact the velocity field and would only appear as a hydrostatic term in the pressure expression. It is thus neglected here. Using cylindrical coordinates  $(r, \theta, z)$  and assuming radial symmetry with the velocity field  $\mathbf{v} = (v_r, 0, 0)$  and  $v_r = v_r(r, z, t)$ , the radial component of eqn (18a) reads

$$\partial_t v_r + v_r \partial_r v_r = -\frac{\partial_r p}{\rho} + \frac{\mu}{\rho} \left[ \partial_r^2 v_r + \partial_z^2 v_r + \frac{\partial_r v_r}{r} - \frac{v_r}{r^2} \right]. \quad (19)$$

The  $\theta$  and  $z$  components of eqn (18a) yield

$$\partial_\theta p = 0 \quad \text{and} \quad \partial_z p = 0. \quad (20)$$

Consequently, the pressure  $p$  depends only on the radial coordinate and time,  $p = p(r, t)$ . The continuity eqn (18b) leads to

$$\frac{1}{r} \partial_r (r v_r) = \partial_r v_r + \frac{v_r}{r} = 0. \quad (21)$$

Using eqn (21) and its first derivative with respect to  $r$ , the Navier–Stokes eqn (19) reduces to

$$\partial_t v_r - \frac{v_r^2}{r} = -\frac{1}{\rho} \partial_r p + \frac{\mu}{\rho} \partial_z^2 v_r. \quad (22)$$

A steady velocity profile for Stokes flow (neglecting the nonlinear term) is then the solution of the following equation

$$\mu \partial_z^2 v_r = \partial_r p, \quad (23)$$

which is readily integrated with the no-slip boundary condition ( $v_r(r, \pm h/2) = 0$ ) to give

$$v_r = \frac{1}{2\mu} \partial_r p \left[ z^2 - \frac{h^2}{4} \right]. \quad (24)$$

The pressure gradient can be related to the flow rate through the relation

$$Q = \int_A v_r(r, z) dA = \int_0^{2\pi} r d\theta \int_{-h/2}^{h/2} v_r(r, z) dz, \quad (25)$$

where  $A$  is the section of reactor along the  $z$ -direction located at a radial distance  $r$ . The integrals are readily performed to give the following pressure profile

$$\partial_r p = -\frac{6\mu Q}{\pi h^3 r}. \quad (26)$$

The radial velocity profile is thus given by

$$v_r(r, z) = \frac{3Q}{\pi h^3 r} \left[ \frac{h^2}{4} - z^2 \right], \quad (27)$$

which coincides with eqn (6) of the main text. The validity of the Stokes approximation can be assessed by analyzing under which condition the nonlinear inertial term can be neglected compared to the viscous term:

$$|\mu \partial_z^2 v_r| \gg \max_{z \in [-h/2, h/2]} \rho \frac{v_r(r, z)^2}{r} = \rho \frac{v_r(r, 0)^2}{r}. \quad (28)$$

Using eqn (27), we find that this condition is equivalent to

$$r \gg \left( \frac{3Q\rho h}{32\pi\mu} \right)^{1/2}. \quad (29)$$

In our case, for the largest value of  $Q$  and  $h$  we consider, the right-hand side is at most equal to 0.2 mm. Hence, the velocity profile (27) is already established very close to the injection valve and a Poiseuille flow is thus indeed operative under our experimental conditions. Finally, the 2D profile adopted by the injected fluid is given by the following ODE,

$$v_r = d_t r = \frac{3Q}{\pi h^3 r} \left[ \frac{h^2}{4} - z^2 \right], \quad r(0) = 0, \quad (30)$$

whose solution can be written as

$$\frac{\bar{r}^2}{2\bar{t}} + \bar{z}^2 = 1, \quad (31)$$

with  $\bar{r} = r/h$ ,  $x = 2\bar{z}/h$ ,  $\bar{t} = t/T$  and  $T = 4\pi h^3/3Q$ . This is the equation of an ellipse centered at the origin of the coordinates and whose radius along the  $r$ -axis, *i.e.*, at  $z = 0$ , grows as

$$\bar{r} = (2\bar{t})^{1/2} \Rightarrow r = \left[ \frac{3Q\bar{t}}{2\pi h} \right]^{1/2}, \quad (32)$$

whereas the radius along the  $z$ -axis stays constant in time and equal to  $h/2$ . Combining eqn (32) with eqn (29), the condition of validity of the Stokes approximation becomes

$$t \gg \frac{\rho h^2}{16\mu}. \quad (33)$$

For the largest solution height used, the right-hand of this last relation is at most equal to 0.03 s. This again shows the need to take the Poiseuille profile (27) into account.

## Acknowledgements

A. T., N. P. D., G. S. and D. H. acknowledge support by the National Research, Development and Innovation Office (NN125746 as ERA-NET) and GINOP-2.3.2-15-2016-00013. A. D. and F. B. acknowledge support by F. R. S.-FNRS under the M-ERA.NET grant no. R.50.12.17.F.

## References

- 1 I. Prigogine and G. Nicolis, *Self-Organization in Nonequilibrium Systems*, John Wiley & Sons, New-York, 1977.
- 2 J. D. Murray, *Mathematical Biology*, Springer-Verlag, Berlin, 2003.

- 3 R. M. Anderson and R. M. May, *Infectious Diseases in Humans: Dynamics and Control*, Oxford University Press, Oxford, 1991.
- 4 *Mathematical Epidemiology*, ed. F. Brauer, P. van den Driessche and J. Wu, Springer-Verlag, Berlin, 2008, vol. 1945.
- 5 G. Cosner, in *Tutorials in Mathematical Biosciences IV*, ed. A. Friedman, Springer, Berlin, 2008, ch. 3, vol. 1922 of *Lecture Notes in Mathematics*, pp. 77–115.
- 6 S. Kondo and T. Miura, *Science*, 2010, **329**, 1616–1620.
- 7 A. Luque and U. Ebert, *Nat. Geosci.*, 2009, **2**, 757–760.
- 8 I. Mastromatteo, B. Tóth and J.-P. Bouchaud, *Phys. Rev. Lett.*, 2014, **113**, 268701.
- 9 D. Toussaint and F. Wilczek, *J. Chem. Phys.*, 1983, **78**, 2642–2647.
- 10 L. Gálfi and Z. Rácz, *Phys. Rev. A: At., Mol., Opt. Phys.*, 1988, **38**, 3151(R)–3154(R).
- 11 Z. Jiang and C. Ebner, *Phys. Rev. A: At., Mol., Opt. Phys.*, 1990, **42**, 7483–7486.
- 12 Y. E. Koo, L. Li and R. Kopelman, *Mol. Cryst. Liq. Cryst.*, 1990, **183**, 187–192.
- 13 Y.-E. L. Koo and R. Kopelman, *J. Stat. Phys.*, 1991, **65**, 893–918.
- 14 S. H. Park, S. Parus, R. Kopelman and H. Taitelbaum, *Phys. Rev. E: Stat., Nonlinear, Soft Matter Phys.*, 2001, **64**, 055102(R).
- 15 F. Brau, G. Schuszter and A. De Wit, *Phys. Rev. Lett.*, 2017, **118**, 134101.
- 16 F. Brau and A. De Wit, *J. Chem. Phys.*, 2020, **152**, 054716.
- 17 J. F. Below Jr., R. E. Connick and C. P. Coppel, *J. Am. Chem. Soc.*, 1958, **80**, 2961–2967.
- 18 J. D. Jackson and G. R. Symmons, *Appl. Sci. Res.*, 1966, **15**, 59–75.
- 19 S. D. R. Wilson, *Appl. Sci. Res.*, 1972, **25**, 349–354.
- 20 G. I. Taylor, *Proc. R. Soc. London, Ser. A*, 1953, **219**, 186–203.
- 21 R. Aris, *Proc. R. Soc. London, Ser. A*, 1956, **235**, 67–77.
- 22 R. N. Horne and F. Rodriguez, *Geophys. Res. Lett.*, 1983, **10**, 289–292.